Alma Mater Studiorum Università di Bologna
Archivio istituzionale della ricerca

Self-assembling, structure and nonlinear optical properties of fluorescent organic nanoparticles in water

(Article begins on next page)

17 December 2025

PCCP

Physical Chemistry Chemical Physics

Accepted Manuscript

Volume 19
Number 1
7 January 2017
Pages 1-896

PCCP

Physical Chemistry Chemical Physics

rsc.li/pccp

ISSN 1463-9076

PAPER
H.-P. Loock et al.
Determination of the thermal, oxidative and photochemical
degradation rates of scintillator liquid by fluorescence EEM
spectroscopy.

ROYAL SOCIETY
OF CHEMISTRY

rsc.li/pccp

ARTICLE TYPE

Self-assembling, structure and nonlinear optical properties of fluorescent organic nanoparticles in water[†]

Laurie Lescos,[a] Pierre Beaujean,[b] Claire Tonnelé,[c] Philippe Aurel,[a] Mireille Blanchard-Desce,[a] Vincent Rodriguez,[a] Marc de Wergifosse,[*d] Benoît Champagne,[*b] Luca Muccioli,[*a,e] and Frédéric Castet[*a]

Owing to their intense emission, low toxicity and solubility in aqueous medium, fluorescent organic nanoparticles (FONs) have emerged as promising alternatives to inorganic ones for the realization of exogenous probes for bioimaging applications. However, the intimate structure of FONs in solution, as well as the role played by intermolecular interactions on their optical properties, remain challenging to study. Following a recent Second-Harmonic Scattering (SHS) investigation led by two of us [Daniel *et al., ACS Photonics*, 2015, **2**, 1209], we report herein a computational study of the structural organization and second-order nonlinear optical (NLO) properties of FONs based on dipolar chromophores incorporating a hydrophobic triphenylamine electron-donating unit and a slightly hydrophilic aldehyde electron-withdrawing unit at their extremities. Molecular dynamics simulations of the FONs formation in water are associated to quantum chemical calculations, to provide insight on the molecular aggregation process, the molecular orientation of the dipolar dyes within the nanoparticles, as well as the dynamical behavior of their NLO properties. Moreover, the impact of intermolecular interactions on the NLO responses of the FONs is investigated by employing the tight-binding version of the recently developed simplified Time-Dependent Density Functional Theory (sTD-DFT) approach, allowing the all-atom quantum mechanics treatment of nanoparticles.

1 Introduction

Imaging technologies play a critical role in biological applications such as cancer detection, stem cell transplantation and tissue engineering. Among them, fluorescence imaging has attracted attention because of its capacity to provide strong signal intensity and high resolution images at subcellular level. Molecular fluorescent dyes are widely used, but are limited by the fact that they contain only a single luminescent center that can absorb and emit a limited number of photons per time and space units. In contrast, fluorescent nanoparticles (NPs) concentrate a huge number of fluorescent centers in a narrow region of space, which enables intense and bright spotlight emission. Therefore in the last decades, nanoparticles have attracted increased interest in biology and optoelectronics fields, in particular luminescent metal- and semiconductor-based nanoparticles. A number of them however raise toxicity and biodegradability issues, which are critical with regard to biomedical applications and environmental concerns. In that perspective, molecular-based fluorescent organic nanoparticles (FONs) emerged as a promising less toxic alternative to inorganic ones, offering appealing ways towards the realization of exogenous probes for biomaging applications.[1-4]

Some years ago, Blanchard-Desce and coworkers reported bright near-infrared emitting FONs made from dipolar push−pull chromophores incorporating a strong electron-withdrawing group.[2] By varying the nature of the electron-accepting unit (among

a Institut des Sciences Moléculaires (ISM, UMR CNRS 5255), University of Bordeaux, 351 Cours de la Libération, 33405 Talence, France.

b Unité de Chimie Physique Théorique et Structurale, Chemistry Department, Namur Institute of Structured Matter, University of Namur, Belgium.

c Donostia International Physics Center (DIPC), Manuel Lardizabal Ibilbidea 4, 20018 Donostia, Euskadi, Spain.

d Mulliken Center for Theoretical Chemistry, Institut für Physikalische und Theoretische Chemie, Beringstr. 4, 53115 Bonn, Germany.

e Department of Industrial Chemistry "Toso Montanari", University of Bologna, Viale Risorgimento 4, 40136 Bologna, Italy.
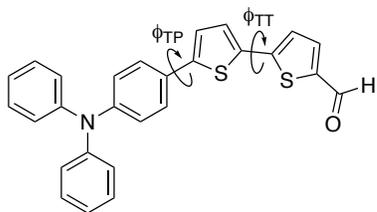
Fig. 1 Chemical structure of the dipolar dye investigated in this work, with the dihedral angles ϕ_{TT} = S-C-C-S and ϕ_{TP} = C-C-C-S.

which the slightly hydrophilic aldehyde as illustrated in Figure 1) and of the π-conjugated systems, FONs showing tuneable emission (from green to NIR) and exhibiting good colloidal stability in water were obtained.[5–7]

The analysis of the fluorescence emission spectra and lifetimes of these nanoparticles suggested possible nanostructuration of dipolar dyes within the FONs, that could result from a specific local organization and orientation of the chromophores in the vicinity of the nanoparticles surface. This hypothesis was further addressed by measuring the second-order nonlinear (NLO) responses of the FONs made from the dipolar dye shown in Figure 1, by means of polarization-resolved Hyper-Rayleigh Scattering (HRS) experiments, which is a powerful selective method to investigate interfacial properties.[8] In contrast to that of constitutive dyes, the measured Second-Harmonic Scattering (SHS) signals of the FONs arise exclusively from the dipolar hyperpolarizability component, with negligible contribution of the octupolar one. These results were attributed to the presence of correlated polar H-type arrangements of the dyes at the water interface, with the hydrophobic triphenylamine end-group pointing toward the center of the NP and the formyl end-group pointing toward water.

The objective of this computational study is to complement these experimental investigations by substantiating or not the results and conclusions that were disclosed for NPs based on the dye sketched on Figure 1. Molecular dynamics simulations of the nanoparticles formation[9–12] in pure water are associated to quantum chemical calculations based on Density Functional Theory (DFT), in order to provide insights on the NPs formation process, the molecular orientation of dipolar dyes within the NPs, as well as the dynamical behavior of their NLO properties. For the first time, the optical response properties of nanoparticles are evaluated fully quantum mechanically by using the tight-binding version of the simplified TD-DFT (sTD-DFT) method, which enables a drastic reduction of computational costs for structures involving several thousands of atoms.[13,14]

2 Computational methods

2.1 Molecular dynamics simulations

Classical MD simulations were carried out using the NAMD software[15] and analyzed with VMD.[16] Organic chromophores were modeled using a modified version of the General AMBER Force Field.[17] Atomic charges were obtained by fitting the electrostatic potential calculated at the B3LYP/cc-pVTZ level of theory, after geometry optimization, using the Gaussian 16 software.[18] The

relaxed B3LYP/cc-pVTZ torsional potentials around the Thienyl-Thienyl and Thienyl-Phenyl dihedrals (ϕ_{TT} and ϕ_{TP}, Figure 1) were calculated and implemented in the force field with the methodology described in Ref. [19]. Water molecules were described by the flexible variant of the simple point charge model (SPC/Fw),[20] which well reflects the dynamical and dielectric properties of bulk water. Details on the parameterization of the force fields are provided in the Electronic Supplementary Information (ESI).

MD simulations were first performed for 1000 ns in the NpT ensemble (p = 1 atm and T = 300 K) by employing periodic boundary conditions with a cubic simulation box containing one single organic dye and 1000 water molecules. The self-aggregation of the dyes was simulated by using a 117.2 Å edge cubic simulation box constituted of 100 dipolar dyes surrounded by 46850 water molecules. The initial random spatial distribution of the organic molecules was obtained using the Packmol software.[21] Then, a MD equilibration procedure was performed on this system for 1 ns within the NpT ensemble and 1 ns within the NVT ensemble, using a temperature of 300 K. To avoid the aggregation of the dyes during this step, the position of their atoms was fixed. In a second step, 8 replicas of the equilibrated system (Figure S3) were created, and used as starting guesses for 8 different MD simulations performed at 300 K for 250 or 300 ns in the NpT ensemble. A multiple time-stepping integration scheme was used, with a time step of 1 fs for the bonded forces, 2 fs for the Lennard-Jones forces and 4 fs for electrostatic ones. A cutoff of 10 Å was used for intermolecular Lennard-Jones interactions, for which standard Lorentz-Berthelot mixing rules were also applied. Long range electrostatic interactions were evaluated with the Particle Mesh Ewald method with a grid spacing of 1.5 Å. Temperature was controlled with the simple velocity scaling algorithm and pressure with Berendsen barostat.

2.2 Calculation of second-order NLO properties

The static and dynamic (frequency-dependent) components of the first hyperpolarizability tensor of single dyes in solution were computed using the time-dependent Density Functional Theory (TD-DFT) at the M06-2X/6-311+G(d) level.[22,23] As evidenced in previous theoretical works, the M06-2X[24] exchange-correlation functional is well suited for calculating the NLO responses of push–pull conjugated dyes, owing to its substantial amount (54%) of long-range Hartree–Fock (HF) exchange.[25,26] Besides, in the case of the chromophore investigated here, M06-2X yields static first hyperpolarizabilities in close agreement with the ones calculated at the second-order Moller-Plesset (MP2) level (see ESI).

Frequency-dependent hyperpolarizabilities were calculated using an incident radiation at 1064 nm (1.16 eV), to match the Q-switched Nd:YAG laser source used in the HRS experiments. Solvent effects were included in all TD-DFT calculations by using the integral equation formalism of the polarized continuum model (IEF-PCM).[27,28] In order to include the effect of geometry fluctuations, NLO responses calculated using molecular geometries optimized at the DFT level were compared to averaged

NLO responses obtained from a statistical sampling of molecular structures extracted at regular time intervals of the MD trajectories. This sequential MD/DFT scheme was used in previous works for evaluating the second-order NLO responses of dyes in solution[29–31] or embedded in complex environments such as biological membranes[32] or self-assembled monolayers.[33,34]

The NLO responses of nanoparticles were calculated using two approaches. The first and crudest approximation consisted in evaluating the first hyperpolarizability of the nanoparticles through the simple summation of the tensor components of the constitutive molecules, using the molecular orientations provided by the MD trajectories. This approach captures the impact of dynamical geometry fluctuations constrained by steric interactions on the NLO properties of the supramolecular structures, but it neglects all mutual polarization effects and intermolecular electronic couplings. In a second step, to take into account these effects, we employed the recently developed sTD-DFT scheme, which provides response properties of large systems at a much lower computational cost than its TD-DFT parent.[13,14] In this framework, the computationally demanding four-index two-electron integrals are approximated using the expression below:

$$(pq|rs) = \sum_A^N \sum_B^N q_{pq}^A q_{rs}^B \Gamma_{AB} \tag{1}$$

where p, q, r, s are the indices of molecular orbitals, q_{pq}^A are transition density monopoles (atomic charges) centered on atom A and Γ_{AB} is the Mataga-Nishimoto-Ohno-Klopman (MNOK) short-range damped Coulomb operator. The latter takes slightly different forms for Coulomb (J) and exchange (K) integrals:

$$\Gamma_{AB}^J = \left(\frac{1}{(R_{AB})^{y_J} + (a_x \eta)^{-y_J}} \right)^{\frac{1}{y_J}} \tag{2}$$

$$\Gamma_{AB}^K = \left(\frac{1}{(R_{AB})^{y_K} + (\eta)^{-y_K}} \right)^{\frac{1}{y_K}} \tag{3}$$

In these expressions, $a_x = 0.54$ is the amount of exact HF exchange in the exchange-correlation functional, η is the mean of the chemical hardness of atoms A and B (whose values are taken from Ref. [35]), and y_J and y_K are two adjustable parameters. In addition to the damping of two-electron integrals, the sTD-DFT scheme also involves a massive truncation of the single-excitation expansion space, by selecting only those below a given energy threshold E_{th}.

To further reduce the computational needs, the tight-binding implementation of the sTD-DFT method (sTD-DFT-xTB), as well as its version restricted to valence molecular orbitals (sTD-DFT-vTB), were used. Note that the sTD-DFT-xTB default parameterization was primarily fitted to globally reproduce excited state properties and not NLO ones. The strategy consists in fitting the adjustable parameters to reproduce reference calculations on small model systems that retain most of the physics of larger structures, giving to the sTD-DFT-xTB method a similar accuracy as the reference one.[13,36] In this spirit, preliminary calculations were performed on the isolated dye as well as on supramolecular clusters containing 12 chromophores, in order to define the optimal values of the y_J, y_K and E_{th} parameters involved in the

sTD-DFT equations with respect to M06-2X/6-311G(d) reference calculations. Because of the rather similar performances of the sTD-DFT-xTB and sTD-DFT-vTB methods for this kind of systems, the less computational-demanding sTD-DFT-vTB approach was selected to perform calculations on the NPs. Optimal sTD-DFT-vTB parameters for the systems investigated here are: $y_J = 0.4$, $y_K = 2.0$ and $E_{th} = 5$ eV (see ESI for the full discussion).

2.3 NLO responses of interest

Comparisons between calculated and experimental second-order NLO properties mainly concern two quantities, namely the total HRS intensity (β_{HRS}) and the depolarization ratio (DR), whose expressions below assume a light beam of frequency ω propagating along the Y direction with a (X,Z) plane of incidence in the laboratory frame:

$$\beta_{HRS} = \beta_{HRS}(-2\omega; \omega, \omega) = \sqrt{\langle \beta_{ZZZ}^2 \rangle + \langle \beta_{ZXX}^2 \rangle} \tag{4}$$

$$DR = \frac{\langle \beta_{ZZZ}^2 \rangle}{\langle \beta_{ZXX}^2 \rangle} \tag{5}$$

$\langle \beta_{ZZZ}^2 \rangle$ and $\langle \beta_{ZXX}^2 \rangle$ are ensemble averages arising from the isotropic distribution of molecular orientations in dilute solutions. These two quantities are related to the scattered HRS intensities obtained when the incident light is vertically polarized (parallel to the Z axis, i.e. for a polarization angle $\Psi = 90°$) and horizontally polarized (parallel to the X axis, with $\Psi = 0°$), respectively. Assuming a more general elliptically polarized incident light and a phase retardation of $\pi/2$ in accordance with the setting used in the experimental study,[8] the intensity of the harmonic light collected perpendicular to the incident beam and vertically (V) polarized, is given by the following expression:[37]

$$I_{\Psi V}^{2\omega} \propto \langle \beta_{ZXX}^2 \rangle \cos^4 \Psi + \langle \beta_{ZZZ}^2 \rangle \sin^4 \Psi$$
$$+ \langle (\beta_{ZXZ} + \beta_{ZZX})^2 - 2\beta_{ZZZ}\beta_{ZXX} \rangle \cos^2 \Psi \sin^2 \Psi \tag{6}$$

The expressions of $\langle \beta_{ZZZ}^2 \rangle$, $\langle \beta_{ZXX}^2 \rangle$ and $\langle (\beta_{ZXZ} + \beta_{ZZX})^2 - 2\beta_{ZZZ}\beta_{ZXX} \rangle$ in terms of molecular β tensor components are provided in ESI (Eqs. S1-S3). In line with experimental measurements, HRS data are further analyzed in the framework of the irreducible spherical representation, which allows to decompose the first hyperpolarizability in terms of dipolar ($\beta_{J=1}$) and octupolar ($\beta_{J=3}$) tensorial components. With this formalism, the three HRS invariants $\langle \beta_{ZZZ}^2 \rangle$, $\langle \beta_{ZXX}^2 \rangle$ and $\langle (\beta_{ZXZ} + \beta_{ZZX})^2 - 2\beta_{ZZZ}\beta_{ZXX} \rangle$ involved in equation 6 can be rewritten as:

$$\langle \beta_{ZZZ}^2 \rangle = |\beta_{J=1}|^2 \left(\frac{9}{45} + \frac{6}{105} \rho^2 \right) \tag{7}$$

$$\langle \beta_{ZXX}^2 \rangle = |\beta_{J=1}|^2 \left(\frac{1}{45} + \frac{4}{105} \rho^2 \right) \tag{8}$$

$$\langle (\beta_{ZXZ} + \beta_{ZZX})^2 - 2\beta_{ZZZ}\beta_{ZXX} \rangle = |\beta_{J=1}|^2 \left(-\frac{2}{45} + \frac{22}{105} \rho^2 \right) \tag{9}$$

where the nonlinear anisotropy parameter $\rho = |\beta_{J=3}|/|\beta_{J=1}|$ denotes the relative magnitude of the octupolar and dipolar contributions to the first hyperpolarizability tensor. In the static limit

$(\omega \to 0)$, the total HRS intensity and depolarization ratio are expressed as:

$$\beta_{HRS} = |\beta_{J=1}|\sqrt{\frac{2}{3}\left(\frac{1}{3}+\frac{1}{7}\rho^2\right)} \qquad (10)$$

$$DR = \frac{9(1+\frac{2}{7}\rho^2)}{1+\frac{12}{7}\rho^2} \qquad (11)$$

and equation 6 becomes:

$$I_{\Psi V}^{2\omega} \propto |\beta_{J=1}|^2 \left(\frac{1}{45}+\frac{4}{105}\rho^2\right)$$
$$\times \left[\cos^4\Psi + (DR)\sin^4\Psi + (7-DR)\cos^2\Psi\sin^2\Psi\right] \qquad (12)$$

All hyperpolarizability values reported in this work are given in atomic units (1 a.u. of $\beta = 3.63 10^{-42}$ m^{4}V$^{-1} = 3.2063 \times 10^{-53}$ C^{3}m^{3}J$^{-2} = 8.641 \times 10^{-33}$ esu) in the T convention, which assumes a Taylor series expansion of the electric molecular dipoles as a function of the applied electric fields.[38]

3   Results and discussion

3.1   Aggregation and structural properties

3.1.1   Aggregation energy of molecular pairs in water

The free-energy profile of a pair of dyes in water was determined as a function of the distance separating their centers of mass, using the dynamically adapted biasing force (ABF) method.[39] As shown in Figure S21, the profile clearly shows a minimum around 5 Å, indicating a tendency for the two molecules to aggregate. The aggregation energy, *i.e.* the free-energy difference between their aggregated and separated states, is equal to -6.2 kcal.mol^{-1}, which demonstrates that even the smallest possible aggregate is thermodynamically more stable than the corresponding solvated molecules. This result suggests that, contrary to the standard cases described by classical nucleation theory (CNT),[40,41] there is no critical nucleus size after which supramolecular clusters become stable. According to CNT, the strong driving force for aggregation also indicates that many nuclei can form in a small volume of water, and that the aggregation rate should be very fast.

3.1.2   Self-aggregation of the dyes in water

As a consequence of the high aggregation rate in water, the dyes, initially randomly dispersed in the simulation box, start to self-assemble in the first few nanoseconds of the simulation. The first-formed molecular clusters merge to form bigger ones until they all aggregate into a single nanoparticle, as shown in Figure 2. However, this process becomes increasingly slow as the size of the aggregates increases, since it is governed by Brownian diffusion that slows down at increasing mass. This is illustrated on Figure 3, which reports the number of nanoparticles and the number of dyes composing the biggest aggregate as a function of the simulation time, for the 8 replicated MD trajectories. Figure 3 also shows that all MD runs lead to complete aggregation in less than 250 ns, giving rise to nanoparticles (NP1-8) composed of 100 dyes each. To ensure good equilibration of the structure of the NPs, MD trajectories were extended at least 50 ns after the

complete dye aggregation, *i.e.* up to 250 ns for replicas NP1, NP3, NP6, NP7 and NP8, and up to 300 ns for NP2, NP3 and NP5.
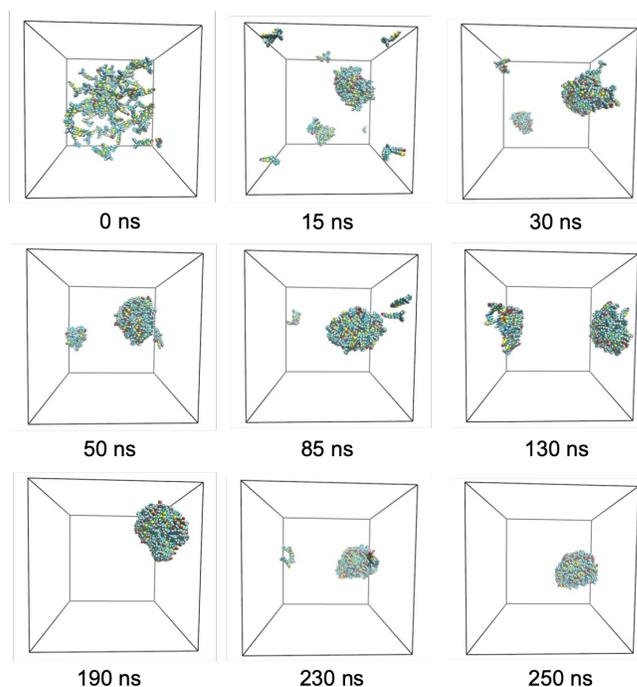

Fig. 2 Snapshots of the simulation box showing supramolecular aggregation over time for NP7. Water molecules are not displayed. A video of the time-evolution of the aggregation is provided in ESI.

3.1.3   Structure of the nanoparticles

The final nanoparticles globally exhibit an ellipsoidal, nearly spherical shape, more or less elongated depending on the replica (see details in ESI), and fluctuating in time (Figures S22 and S23). The orientation of the dipolar dyes within a typical NP structure is illustrated on Figure 4. Not surprisingly, the hydrophobic triphenylamine groups of the dyes mainly point toward the center of the NP, while the hydrophilic formyl groups point towards the outside. This preferential orientation is also illustrated in the graph of Figure 4, which reports the concentration of the different atomic groups as a function of the distance from the NP center.

Interestingly, the time evolution of the average total dipole moment (Figure S25) shows that the NPs have a strong polar character (50 D *vs* 6.5 D for the isolated molecule), further evidencing their non-centrosymmetric shape and distribution of molecular orientations. This is also clearly illustrated in Figure 4 by the map of the electrostatic potential of NP1, calculated from the atomic charge distribution. Moreover, Figure 4 also highlights the presence of domains involving several π-stacked dyes. A statistical analysis of these aggregates, conducted over the 8 final NPs, is detailed in the ESI. It reveals that more than 80% of the molecules within a NP develop π-stacking interactions with at least one of their direct neighbour, through at least one of the three central conjugated rings (Figure S28). The size of the π-stacked domains is comprised between 2 and 20 molecules. A detailed picture of
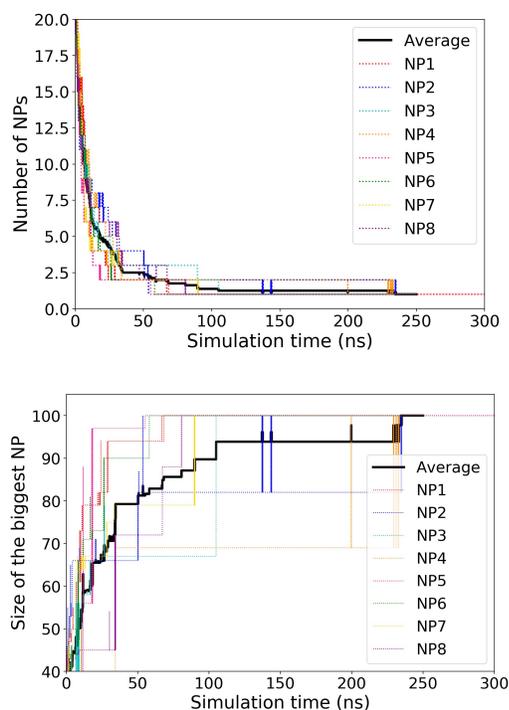
Fig. 3 Evolution of the number of NPs (top) and of the size of the biggest NP (bottom) with simulation time for the 8 replicated MD simulations. Abrupt rises in the evolution are due to the coalescence of two "large" aggregates. Two molecules are considered to be in the same aggregate if at least a couple of non-hydrogen atoms is closer than 4.0 Å.

Fig. 4 Top Left: Example of ellipsoidal nanoparticle composed of 100 aggregated dyes highlighting the orientation of formyl groups (in red) towards the outside, and the π-stacked domains (in yellow); Top Right: Electrostatic portential calculated from the atomic charge distribution (isovalues range from -4 (blue) to $+4$ (red), in kT/e units, with T = 300 K); Bottom: radial number density of the different molecular moieties as a function of the distance from the center of the nanoparticle. Values averaged over the 100 molecules of the 8 final nanoparticles (NP1-NP8).

the relative orientation of π-stacked molecular pairs is provided in Figure S29, which evidences that 35% of the dimers adopt a parallel orientation, consistent with the preferential orientation of the hydrophobic triphenylamine termination towards the center of the NPs. However, it is also found that a significant amount (29%) of the dimers stack antiparallelly, as a result of stabilizing electrostatic interactions, or even in herringbone-like (16%) or cross (22%) configurations.

To further characterize the morphology of the NPs at the atomistic scale, statistical distributions of intra- and intermolecular structural parameters were calculated for the 8 replicas along the last 50 ns of the MD trajectories, *i.e.* after full aggregation of all dyes. Figure 5 illustrates the distribution of the torsional angle ϕ_{TT} associated to the *cis* ($\phi_{TT} = 0°$) or *trans* ($\phi_{TT} = 180°$) configuration of the bithiophene unit (Figure 1), for a single dye in water and for aggregated dyes. In the case of the isolated dye, the probability distribution of ϕ_{TT} values shows two maxima with equal amplitude at $0°$ and $180°$, indicating that *cis* and *trans* configurations are equiprobable, consistently with the close energies of the two isomers and the low rotational energy barriers around the single bond connecting the thienyl groups (Figure S2a). The relative magnitude of the two peaks is slightly modified within the NPs, with the *cis* configuration increasing its probability at the expense of the *trans* one. However, the variations with respect to the isolated dye are weak, indicating that aggregation hardly affects the configurational isomerism of the dipolar
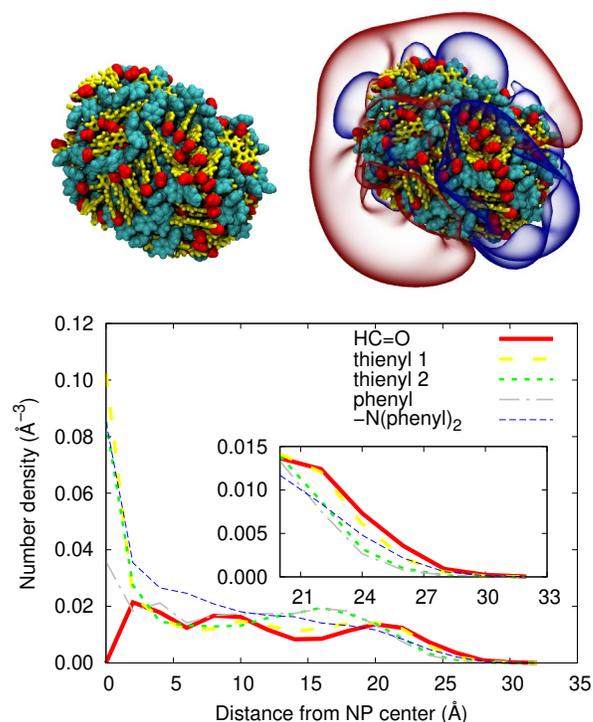
dyes. The same observation holds true regarding the ϕ_{TP} dihedral angle, which describes the rotation around the single bond connecting the thienyl and phenyl groups (Figure 1). The time auto-correlation functions (ACFs) of ϕ_{TT} and ϕ_{TP} angles, calculated for the isolated and aggregated dyes, are plotted in Figure 6. The ACF decays provide the time scale of the rotational motions about the thienyl-thienyl and phenyl-thienyl bonds. Compared to molecules in water solution, the ACFs of molecules inserted in nanoparticles show a much slower decay time (approximately 30 ns, versus 1 ns in solution), owing to the sterically hindered environment, but also show that these intramolecular rotations are still possible.

The evolution of the mean density of neighbours within the nanoparticles as a function of the distance r_{ij} between the centers of mass of molecules (Figure 7) reveals that first molecular neighbours are located at average distances of about 6 Å. Note that after 50 Å, $N(r_{ij})$ falls to zero as the distance exceeds the size of the aggregate (Figure S26), which allows to estimate the average diameter of the NPs to about 5 nm. The evolution of the mean cosine of the angle θ_{ij} between molecular dipoles, also plotted in Figure 7, gives complementary information on the orientation of the molecules within the NPs, with positive (negative) values corresponding to parallel (antiparallel) orientation. As shown in Figure 7, $\langle \cos\theta_{ij} \rangle$ is positive at the first neighbours distance, suggest-
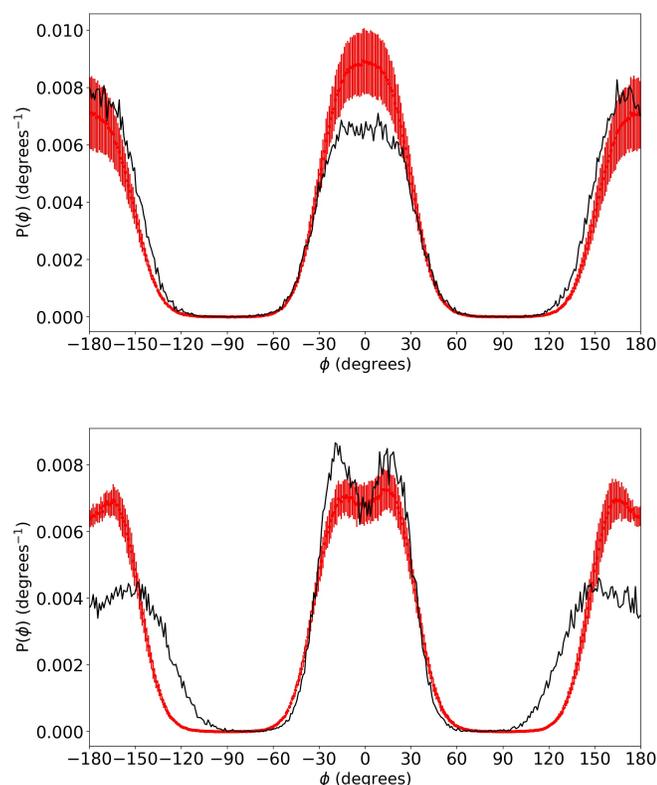
Fig. 5 Distribution of the ϕ_{TT} (top) and ϕ_{TP} (bottom) dihedral angles (Figure 1) for a single dye in water solution (in black, monitored over 1000 ns) and embedded into a nanoparticle (in red, averaged for the 100 constitutive dyes of the 8 final NPs, over the last 50 ns).

Fig. 6 Time autocorrelation function of the dihedral angles ϕ_{TT} and ϕ_{TP} dihedrals, defined as $C(\phi_i) = \langle \cos[\phi_i(t) - \phi_i(0)] \rangle = \langle \cos[\phi_i(0)] \cos[\phi_i(t)] \rangle + \langle \sin[\phi_i(0)] \sin[\phi_i(t)] \rangle$, calculated for the isolated and aggregated dyes.

ing a parallel orientation between first neighbours, which is at the origin of the overall non-zero dipole moments of the NPs (Figure S25). At larger distances, $\langle \cos \theta_{ij} \rangle$ approaches zero, indicating that this correlation is lost. The short range preferential parallel ordering of the dipolar dyes is confirmed by the distribution of $\langle \cos \theta_{ij} \rangle$ values for molecules closer than 7.5 Å (Figure S27), which shows a weak maximum for $\langle \cos \theta_{ij} \rangle = 1$. Note that the distribution displays a second maximum at $\langle \cos \theta_{ij} \rangle = -1$, showing the propensity of neighbouring chromophores to also stack with an anti-antiparallel configuration.

3.2 Nonlinear optical properties

3.2.1 NLO responses of solvated dyes

The dynamic HRS properties calculated at the DFT level for the *cis* and *trans* forms of the isolated molecule (as well as "averaged" values estimated using relative *trans/cis* Boltzmann populations at room temperature) are compared to those measured in dilute chloroform and acetonitrile solutions in Table 1. Although the computed HRS hyperpolarizabilities are about three times larger than the experimental ones, the slight enhancement of the β_{HRS} values from chloroform to acetonitrile is well reproduced. DFT calculations performed in water show that increasing further the solvent polarization effects has no impact on the NLO proper-
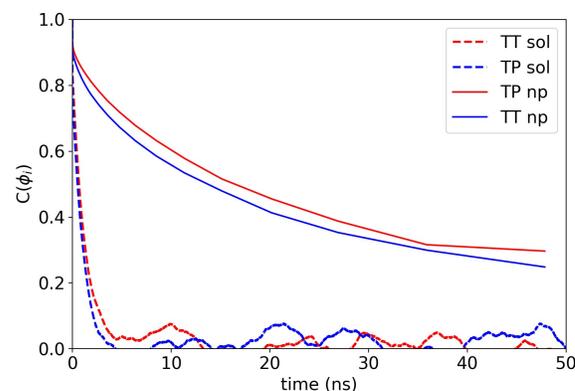
ties of the dye. Unlike experimental results which show that the NLO response of the dye in chloroform is slightly dominated by its octupolar contribution ($\rho > 1$), DFT calculations predict a low predominance of dipolar character in both solvents, with weak solvatochromism effect. This small discrepancy likely originates from the theoretical treatment of solute-solvent interactions by means a continuum solvation model, where intermolecular interactions are not treated explicitly. DFT calculations and HRS measurements are further compared on the polar plots showing the evolution of the harmonic light intensity as a function of the polarization angle Ψ of the incident beam (Figure 8). In acetonitrile, the theoretical curve calculated using Eq. 12 quasi perfectly matches the experimental fits, while the agreement is worse for data in chloroform, where the thinner shape of the theoretical curve reveals an overestimated dipolar character. Note that part of the discrepancy between experimental and theoretical data might also arise from the lower quality of the experimental fits in the $\Psi = 0°$ and $\Psi = 180°$ zones. Moreover, the large overestimate of calculated β_{HRS} values compared to experiments in both chloroform and acetonitrile may also arise from the increased probability of the formation of small molecular aggregates with a pseudo centrosymmetrical shape (*e.g.* stacked dimers, for which a head-to-tail relative orientation is favored by the dipole-dipole interactions and the better overlap between the conjugated cores).

To gain insight on the impact of thermally-induced geometry distortions, we also compare in Table 1 the NLO properties calculated using the DFT-optimized geometries of the dye in water solution to those averaged over 100 molecular geometries extracted from MD trajectories (MD+DFT). The two approaches provide similar DR and ρ values, suggesting that structural fluctuations do not induce significant change in the multipolar character of the NLO responses. On the contrary, the MD-averaged β_{HRS} values show a 30% decrease compared to DFT ones. This is consistent with the low energy barriers for the rotation around the Thienyl-Thienyl and Thienyl-Phenyl bonds (Figures S1 and S2). In fact, many structures extracted from MD runs display

Table 1 Total dynamic HRS hyperpolarizabilities (β_{HRS}), dipolar ($|\beta_{J=1}|$) and octupolar ($|\beta_{J=3}|$) components (all values in 10^3 a.u.), as well as the associated depolarization (DR) and anisotropy (ρ) ratios deduced from HRS measurements at 1064 nm in chloroform (chl) and acetonitrile (ace), and calculated at the DFT level in chloroform and acetonitrile, and at the DFT and MD+DFT levels in water.

	β_{HRS}	DR	ρ	$|\beta_{J=1}|$	$|\beta_{J=3}|$
Exp.[a] (chl)	12.5	3.6	1.22 ± 0.03	20.7	25.3
DFT[b] (*trans*,chl)	37.5	4.8	0.85	69.5	59.2
DFT[b] (*cis*,chl)	32.3	5.0	0.82	60.4	49.5
DFT[b,c] (*av*,chl)	34.1	4.9	0.83	63.5	52.9
Exp.[a] (ace)	13.3	4.6	0.91 ± 0.03	24.2	22.0
DFT[b] (*trans*,ace)	37.9	4.9	0.85	70.3	59.6
DFT[b] (*cis*,ace)	34.2	5.0	0.82	63.9	52.2
DFT[b,c] (*av*,ace)	36.7	4.9	0.83	63.5	52.9
DFT[b] (*trans*,water)	38.0	4.9	0.85	70.5	59.7
DFT[b] (*cis*,water)	34.1	5.0	0.82	63.9	52.2
DFT[b,c] (*av*,water)	36.7	4.9	0.84	63.8	57.2
MD+DFT[d] (water)	28.3 ± 14.7	5.0 ± 0.1	0.83 ± 0.03	52.7 ± 27.3	43.8 ± 22.7

[a] Taken from Ref. 8.
[b] IEFPCM:M06-2X/6-311+G(d) calculations using the IEFPCM:B3LYP/cc-pVTZ geometries.
[c] *av*: averaged values estimated using relative *trans/cis* Boltzmann populations at room temperature.
[d] Averaged over 100 molecular geometries extracted from the MD trajectories.

non planar shapes, corresponding to lower conjugation along the molecular backbone and damped second-order NLO response. A similar decrease of the β_{HRS} response when moving from DFT to MD+DFT calculations was observed previously for a push-pull indolino-oxazolidine derivative also incorporating a bithiophene unit.[29,42] The strong impact of the dynamical fluctuations is further testified by the large standard deviation of the β_{HRS} values.

3.2.2 NLO responses of the nanoparticles

In a first approach, we estimated the first hyperpolarizability tensor of the NPs as the sum of the tensors of the individual constitutive dyes calculated at the TD-DFT level. As mentioned above, although this approximation neglects intermolecular electronic couplings and polarization effects on the NLO properties, it integrates the effects related to the spatial organization of the dyes within the NPs, and to their geometrical fluctuations. As reported in Table S4, static first hyperpolarizabilities for NP1-8 are spread over a broad range of values, as reflected in the large standard deviation of their distributions $\langle\beta_{HRS}\rangle = (43.8 \pm 11.9)10^3$ a.u. As a result of frequency-dispersion effects, dynamic β_{HRS} values are about three times larger than the static ones ($\langle\beta_{HRS}\rangle = (189.1 \pm 70.5)10^3$) a.u. with a larger distribution (Table 2). The impact of frequency dispersion on the depolarization ratios is less systematic, either increasing or decreasing the DR values depending on the considered NP. Despite these irregular fluctuations, the average static and dynamic depolarization ratios are very close (4.5-4.6), indicating that the NLO responses of the supramolecular structures globally exhibit a 1D character, typical of systems for which the hyperpolarizability tensor is dominated by a single diagonal component.

Data reported in Table S6 and Figure S31 show that the NLO responses of individual nanoparticles also display large fluctuations with respect to dynamical geometry fluctuations along the MD simulation. The evolution over time of the cumulative averages of β_{HRS} and DR values is illustrated in Figure 9 for NP5,

starting from the time (140 ns) where the 100 molecular dyes collapse into a single structure. Even though individual values vary strongly over time, the cumulative averages rapidly converge to $\langle\beta_{HRS}\rangle = 204.10^3$ a.u. and $\langle DR\rangle = 4.3$.

With the exception of NP7, the static β_{HRS} and DR values evaluated using the tensor-sum approximation at the sTD-DFT-vTB level are very close to those estimated using the full-featured TD-DFT level (the R_1 ratios in Table S4 and the linear correlation in Figure S30). In the case of dynamic calculations, the average β_{HRS} value obtained with sTD-DFT-vTB is 1.7 times larger than the TD-DFT one (Table 2), while the mean DR value increases from 4.6 to 5.0.

Comparing sTD-DFT-vTB data evaluated using the tensor-sum approximation with those issued from calculations on the whole supramolecular structure provides a direct measure of the effects of intermolecular interactions. In the static case, a good correspondence is found between the two sets of values (Figure S30), while accounting for intermolecular interactions induces a 20% lowering of the HRS hyperpolarizability. As evidenced in the case of π-stacked dimers (Table S6 and Figure S33), this decrease can be ascribed to the slight blue-shift of the main absorption band upon aggregation of the dyes. On the contrary, as a result of resonance effects, dynamic β_{HRS} values display very large and non systematic variations, going from a $\sim 80\%$ decrease for NP7 to a $\sim 900\%$ increase for NP1. Considering data averaged over the 8 NPs, intermolecular interactions enhance the dynamic β_{HRS} response by about a factor 3, while the DR value is lowered from 5.0 to 4.2. We stress however that the very large β_{HRS} values calculated for NP1 and NP4, and therefore the average β_{HRS} value, should be taken with caution, since the response functions diverge at the harmonic frequency inducing numerical instabilities. These results also highlight the important effects of intra and intermolecular structural variations, which reflect in the large standard deviation of the NLO responses. As reported in Table S6, the relative standard deviations on β_{HRS} calculated for the 8 repli-
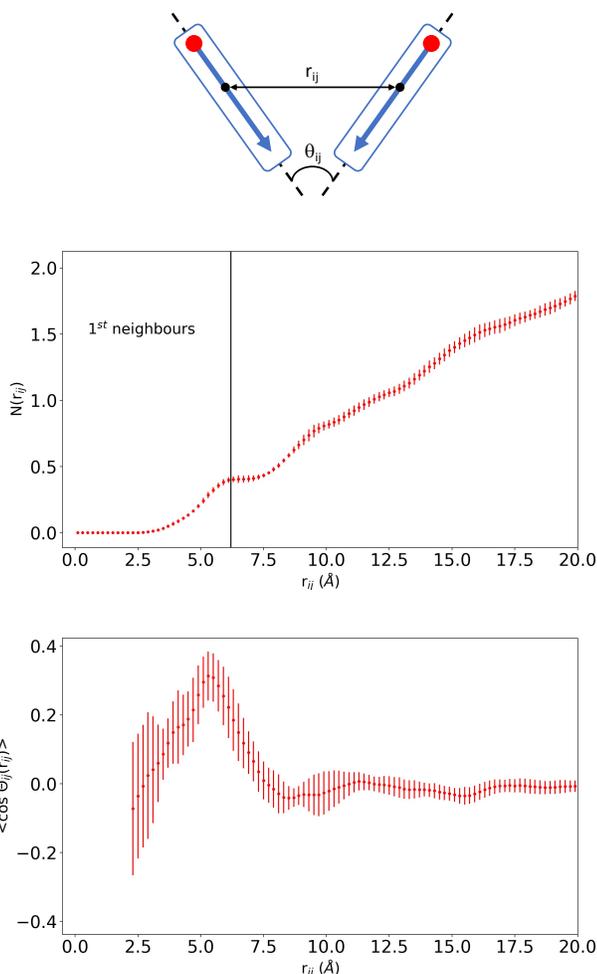
Fig. 8 Normalized polar representations of the evolution of the harmonic light intensity as a function of the polarization angle Ψ of the incident beam, as measured in chloroform (left) and acetonitrile (right). Red circles correspond to measured values. Red lines are the best experimental fitted curves. Black lines are calculated using Eq. 12 with β-components calculated at the IEFPCM:M06-2X/6-311+G(d) level.

Fig. 9 Time evolution of β_{HRS} (left) and DR (right) values for NP5 (empty dots) and of their cumulative moving averages (full dots), as calculated using the tensor-sum approximation at the TD-DFT:M06-2X/6-311+G(d) level.

Fig. 7 Definition of the angle θ_{ij} between molecular dipoles and the distance r_{ij}, between molecular centers of mass (top), and evolution of the mean density of neighbours $N(r_{ij})$ (middle) and of the mean cosine of θ_{ij} (bottom) as a function of r_{ij}.

cated MD trajectories range from 22% to 47%, and are of similar magnitude (from 26% to 48%) for the depolarization ratio.

3.3 Absorption properties

In order to investigate further the origin of the large enhancement of the dynamic NLO response upon molecular aggregation, we investigated the absorption properties of the dyes in their isolated and aggregated states. In a first step, the vertical excitation energies and oscillator strengths towards low-lying excited states were calculated for three representative π-stacked dimers extracted from the NPs (Figure S31). As reported in Table S7 and Figure S33, TD-DFT calculations performed at the M06-2X/6-311+G(d) level show that, compared to the isolated monomer, dipole-allowed red-shifted transitions appear in the three dimerized structures. Additional calculations using a Boys localization scheme[43] to decompose the electronic eigenstates into a set of pure (diabatic) intramolecular and intermolecular charge-transfer (CT) electronic configurations further evidenced that some low energy electronic transitions with large oscillator
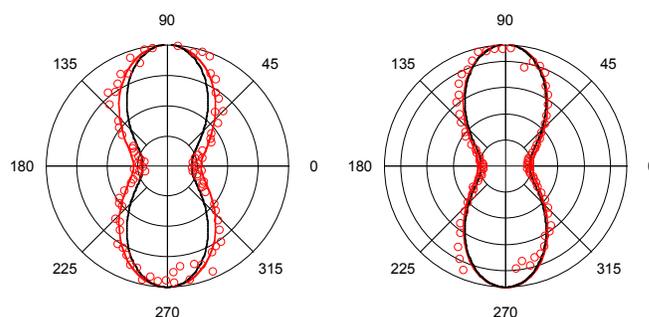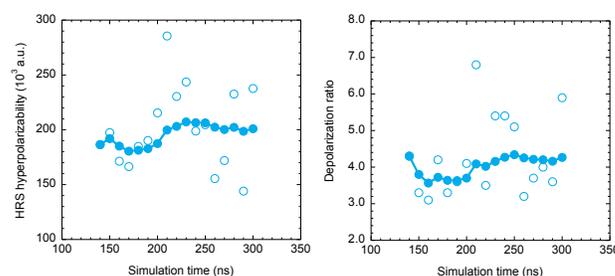
strength have a dominant intermolecular CT character (see details in ESI). As also shown in Table S7 and Figure S33, despite a global blue-shift of the main absorption bands compared to TD-DFT, the appearance of these new low-energy excited states is qualitatively well reproduced by sTD-DFT-vTB calculations using the same y_J, y_K and E_{th} parameters as those used in NLO calculations.

In a second step, we thus calculated the electronic excited states of a representative NP composed of 100 chromophores using the same sTD-DFT-vTB scheme. The absorption spectrum of the NP (Figure 10) is much wider than that of the isolated dye, owing to the structural variety of the constitutive molecular units and, as shown above, the possibility of intermolecular CT excitations.[44,45] The global shape of the absorption spectrum is fully consistent with the one measured for FON suspensions in water (see Figure 4 of Ref. 5), which exhibits a red-shifted and broadened main absorption band as compared to dyes dissolved in organic solvents, as well as a residual absorption in the long-wavelength region (500-550 nm $\equiv$ 2.25-2.50 eV). These low-energy absorption bands, in part attributed to intermolecular CT excitations, resonate with the second harmonic light at 532 nm (2.32 eV) and are thus at the origin of the enhancement of the dynamic β_{HRS} response upon aggregation.

Table 2 Dynamic (λ = 1064 nm) first hyperpolarizabilities (β_{HRS} in 10^3 a.u.) and depolarization ratios (DR) of the final nanoparticles issued from the 8 replicated MD trajectories, evaluated using the tensor sum approximation at the TD-DFT and sTD-DFT-vTB levels, as well as from sTD-DFT-vTB caculations performed on the whole nanoparticles.

	TD-DFT[a] (tensor sum)		sTD-DFT-vTB[b] (tensor sum)		sTD-DFT-vTB[b] (full calculation)	
	β_{HRS}	DR	β_{HRS}	DR	β_{HRS}	DR
NP1	317.0	6.3	325.8	5.8	3194.5	4.8
NP2	112.0	3.7	248.2	3.4	106.4	3.0
NP3	110.7	3.0	161.2	3.8	616.9	3.6
NP4	160.1	5.1	238.9	5.2	2259.4	5.1
NP5	237.6	5.9	343.1	7.2	369.9	4.7
NP6	185.0	3.6	238.7	4.5	212.7	4.9
NP7	234.0	3.4	827.6	5.0	156.6	2.1
NP8	156.4	5.5	167.9	5.3	634.3	5.0
av.± std. dev.	189.1 ± 70.5	4.6 ± 1.3	318.9 ± 215.4	5.0 ± 1.2	943.8 ± 1145.4	4.2 ± 1.1

[a] M06-2X/6-311+G(d) in gas phase.
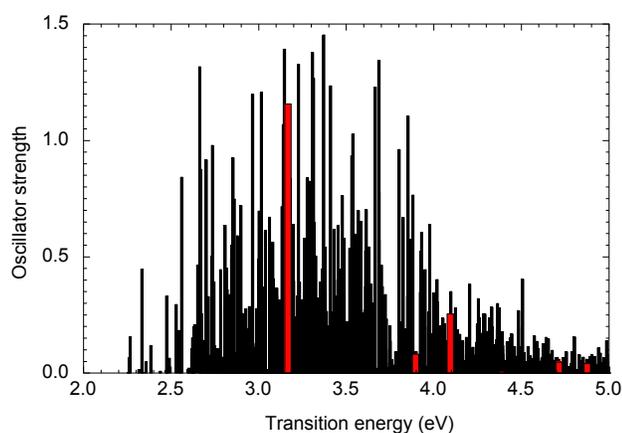[b] Using $y_J = 4.0$, $y_K = 2.0$ and $E_{th} = 5.0$ eV.

Fig. 10 Electronic transitions towards the excited states in NP1 (black bars) and in the *trans* isolated dye (red bars), as calculated at the sTD-DFT-vTB level.

3.4 Comparison to experiments and further discussion

With respect to experiments, this computational study offers complementary insights on the origin of the NLO properties of the molecular-based NPs that are worth being discussed. As reported in Ref. [8], the total second-harmonic signal radiated by the nanoparticles in solution can be partitioned in two contributions, respectively ascribed to the bulk and interfacial areas of the NPs:

$$\beta_{NP} = \beta_{bulk} + \beta_{interf} \qquad (13)$$

The bulk contribution is related to the NLO response of molecular dyes constituting the inner shell of the nanoparticules, *i.e.* not directly in contact with water molecules. A comparison with the three orders of magnitude larger hyperpolarizabilities measured for noncentrosymmetric $BaTiO_3$ or $PbTiO_3$ ferroelectric nanocrystals with comparable diameters, suggests that the NPs investigated here exhibit a negligible β_{bulk} contribution.[46] On the contrary, owing to their limited size, the NPs issued from the simulations can be considered as having no bulk, with all organic dyes being part of the interfacial region.

The interfacial term in equation [13] results from second-order and

third-order contributions:

$$\beta_{interf} = \beta + (\gamma\phi_0)_{EFISH} \qquad (14)$$

The second-order term, β, was previously attributed to the locally non-centrosymmetric H-type structuring of the dyes at the water interface.[8] Our MD simulations confirmed such a specific arrangement, as resulting of π-stacking interactions between the central conjugated rings (Figure [4]). The second term, referred to as electric field induced second harmonic (EFISH), involves the third-order hyperpolarizability (γ) of the chromophores (which is expected to be strong for such two-photon absorbing dyes) and the interfacial local electric field ϕ_0, arising from the surface charge density. It is important to note that this term is neglected in the tensor sum approximation, which only considers the second-order ($\beta \equiv \beta_{HRS}$) contribution. On the contrary, sTD-DFT calculations are in principle able to capture the full NLO response of the NPs, including the third-order contribution. However, since water molecules in the interfacial area are not included in the calculations, the magnitude of local field effects is likely underestimated, and so for the third-order response. Note also that the water molecules in the vicinity of the NP are expected to be partially aligned by the electric field of the charged interface, and thus to contribute themselves to the EFISH response. However, the latter contributions due to water molecules is weak and cannot be detected by an experimental setup featuring a picosecond excitation laser source as used in Ref. [8]. Therefore, only the NLO signal due to the organic dyes is accounted for in the $\beta_{NP} = (3700 \pm 37)10^3$ a.u. value issued from SHS measurements.

The calculated NLO response of nanoparticles in water is about 30 times larger than that calculated for a single molecular dye. This result is consistent with SHS measurements, although the experimental β_{NP}/β_{dye} ratio is one order of magnitude larger. The underestimate of the simulated β_{NP} is directly related to the smaller size of the nanoparticles (of average diameter ∼5 nm *versus* 36 nm for the experimental one, *i.e.* with a surface area approximately 50 times smaller) and to the incomplete treatment of local field effects in equation [14].

For the same reasons, the DR values predicted by sTD-DFT-vTB calculations, ($DR_{NP} = 4.2 \pm 1.1$), are also underestimated com-

pared to SHS measurements ($DR_{NP} = 8.7 \pm 0.9$). As detailed in Ref. 8, it is worth mentioning here that SHS measurements of NPs are expected to generate interferences between the partial waves scattered by the individual molecules, inducing retardation effects at the fundamental and harmonic frequencies. This collective coherent signal, which scales quadratically with the number of correlated molecules, becomes rapidly dominant over the non-coherent one as the size of the nanoparticle increases. In the present case, the very high experimental DR value is partly attributed to the coherent part of the NLO signal, while calculations do not account for any phase relation between the NLO signals scattered by the various molecules.

Finally, an additional difficulty in comparing theory and experiment lies in the need to include the vibrational contributions, the so-called zero-point vibrational averaging.[47] In principle, the MD+DFT computational scheme is able to catch, within the simulation time scale, the effect of molecular vibrations, often causing large fluctuations of the NLO responses. The impact of low energy phonon-like modes, associated to global variations in the shape of the nanoparticles, is also taken into account since NLO properties are calculated as averages over several independent trajectories.

4 Conclusions and perspectives

The molecular dynamics simulations reported here confirm the spontaneous formation of amorphous nanoparticles based on organic dipolar dyes in water solution, as well as the onset of polar π-stacked domains at the water interface. The soft nature of the nanoparticles allows for rather large shape variations, which are reflected in large fluctuations in time of their second-order NLO responses.

The measured strong enhancement of the first hyperpolarizability upon aggregation of the dyes is well reproduced by the tight-binding implementation of the sTD-DFT method, here employed for the first time to characterize the NLO properties of nanoparticles while fully accounting for their dynamical fluctuations through a sequential MD+QM scheme. This approach allowed to evidence the high impact of mutual polarization effects and intermolecular couplings on the NLO responses. In particular, intermolecular interactions are at the origin of the emergence of low-lying excited states entering into resonance with the second harmonic light. These states are responsible for the high enhancement of the SHS signal upon dyes aggregation.

This work also points the difficulty of comparing the calculated and experimental NLO responses of such large and flexible supramolecular assemblies. Limitations of the computational methodology are mainly related to the timescale and size of the objects that can be investigated, to numerical instabilities due to resonance effects, as well as to the probable underestimate of the magnitude of local electric fields since the first solvation shell is not taken into account.

Therefore, this work should be seen as a first step towards accurate simulations of NLO responses of large molecular-based architectures, paving the way toward future calculations and method development. Explicitly including in the calculation the first shell of water molecules close to the NP interface, which, at least for small particles, may be essential for the quantitative prediction of

the EFISH signal, comes out as a natural outlook. The implementation of damped response functions[48-50] within the sTD-DFT scheme would also be of great interest in order to avoid disproportionate resonances. Alternatively, the development of parameterized models on the basis of natural response orbitals would allow investigating larger clusters at low computational cost. Finally, an exhaustive study of the NLO responses of nanoparticles of different sizes would provide insights on the relative magnitude of bulk and interfacial contributions.

Conflicts of interest

There are no conflicts to declare.

Acknowledgements

Notes and references

1 S. Fery-Forgues, Fluorescent organic nanocrystals and non-doped nanoparticles for biological applications, *Nanoscale*, 2013, **5**, 8428–8442.

2 E. Genin, Z. Gao, J. Varela, J. Daniel, T. Bsaibess, I. Gosse, L. Groc, L. Cognet and M. Blanchard-Desce, "Hyper-bright" near-infrared emitting fluorescent organic nanoparticles for single particle tracking, *Adv. Mater.*, 2014, **26**, 2258–61, 2257.

3 P. Xing and Y. Zhao, Multifunctional Nanoparticles Self-Assembled from Small Organic Building Blocks for Biomedicine, *Adv. Mater.*, 2016, **28**, 7304–7339.

4 M. Rosendale, J. Flores, C. Paviolo, P. Pagano, J. Daniel, J. Ferreira, J.-B. Verlhac, L. Groc, L. Cognet and M. Blanchard-Desce, A Bottom-Up Approach to Red-Emitting Molecular-Based Nanoparticles with Natural Stealth Properties and their Use for Single-Particle Tracking Deep in Brain Tissue, *Advanced Materials*, 33, 2006644.

5 V. Parthasarathy, S. Fery-Forgues, E. Campioli, G. Recher, F. Terenziani and M. Blanchard-Desce, Dipolar versus Octupolar Triphenylamine-Based Fluorescent Organic Nanoparticles as Brilliant One- and Two-Photon Emitters for (Bio)imaging, *Small*, 2011, **7**, 3219–3229.

6 K. Amro, J. Daniel, G. Clermont, T. Bsaibess, M. Pucheault,

E. Genin, M. Vaultier and M. Blanchard-Desce, A new route towards fluorescent organic nanoparticles with red-shifted emission and increased colloidal stability, *Tetrahedron*, 2014, **70**, 1903–1909.

7 C. Mastrodonato, P. Pagano, J. Daniel, M. Vaultier and M. Blanchard-Desce, Molecular-Based Fluorescent Nanoparticles Built from Dedicated Dipolar Thienothiophene Dyes as Ultra-Bright Green to NIR Nanoemitters, *Molecules*, 2016, **21**, year.

8 J. Daniel, F. Bondu, F. Adamietz, M. Blanchard-Desce and V. Rodriguez, Interfacial Organization in Dipolar Dye-Based Organic Nanoparticles Probed by Second-Harmonic Scattering, *ACS Photonics*, 2015, **2**, 1209–1216.

9 B. G. Levine, D. N. LeBard, R. DeVane, W. Shinoda, A. Kohlmeyer and M. L. Klein, Micellization Studied by GPU-Accelerated Coarse-Grained Molecular Dynamics, *J. Chem. Theory Comput.*, 2011, **7**, 4135–4145.

10 D. L. Silva, N. A. Murugan, J. Kongsted, H. Ågren and S. Canuto, Self-Aggregation and Optical Absorption of Stilbazolium Merocyanine in Chloroform, *J. Phys. Chem. B*, 2014, **118**, 1715–1725.

11 O. A. Guskova, S. R. Varanasi and J.-U. Sommer, C60-dyad aggregates: Self-organized structures in aqueous solutions, *J. Chem. Phys.*, 2014, **141**, 144303.

12 T. D. Potter, M. Walker and M. R. Wilson, Self-assembly and mesophase formation in a non-ionic chromonic liquid crystal: insights from bottom-up and top-down coarse-grained simulation models, *Soft Matter*, 2020, **16**, 9488–9498.

13 M. de Wergifosse and S. Grimme, Nonlinear-response properties in a simplified time-dependent density functional theory (sTD-DFT) framework: Evaluation of the first hyperpolarizability, *J. Chem. Phys.*, 2018, **149**, 024108.

14 M. de Wergifosse and S. Grimme, Perspective on Simplified Quantum Chemistry Methods for Excited States and Response Properties, *J. Phys. Chem. A*, 2021, **125**, 3841–3851.

15 P. J. C., B. Rosemary, W. Wei, G. James, T. Emad, V. Elizabeth, C. Christophe, S. R. D., K. Laxmikant and S. Klaus, Scalable molecular dynamics with NAMD, *J. Comput. Chem.*, 2005, **26**, 1781–1802.

16 W. Humphrey, A. Dalke and K. Schulten, VMD: Visual molecular dynamics, *J. Mol. Graphics*, 1996, **14**, 33–38.

17 J. Wang, R. M. Wolf, J. W. Caldwell, P. A. Kollman and D. A. Case, Development and testing of a general amber force field, *J. Comput. Chem.*, **25**, 1157–1174.

18 M. J. Frisch, G. W. Trucks, H. B. Schlegel, G. E. Scuseria, M. A. Robb, J. R. Cheeseman, G. Scalmani, V. Barone, G. A. Petersson, H. Nakatsuji, X. Li, M. Caricato, A. V. Marenich, J. Bloino, B. G. Janesko, R. Gomperts, B. Mennucci, H. P. Hratchian, J. V. Ortiz, A. F. Izmaylov, J. L. Sonnenberg, D. Williams-Young, F. Ding, F. Lipparini, F. Egidi, J. Goings, B. Peng, A. Petrone, T. Henderson, D. Ranasinghe, V. G. Zakrzewski, J. Gao, N. Rega, G. Zheng, W. Liang, M. Hada, M. Ehara, K. Toyota, R. Fukuda, J. Hasegawa, M. Ishida, T. Nakajima, Y. Honda, O. Kitao, H. Nakai, T. Vreven, K. Throssell, J. A. Montgomery, Jr., J. E. Peralta, F. Ogliaro, M. J. Bearpark, J. J.

Heyd, E. N. Brothers, K. N. Kudin, V. N. Staroverov, T. A. Keith, R. Kobayashi, J. Normand, K. Raghavachari, A. P. Rendell, J. C. Burant, S. S. Iyengar, J. Tomasi, M. Cossi, J. M. Millam, M. Klene, C. Adamo, R. Cammi, J. W. Ochterski, R. L. Martin, K. Morokuma, O. Farkas, J. B. Foresman and D. J. Fox, Gaussian 16 Revision C.01, 2016.

19 A. Pizzirusso, M. E. Di Pietro, G. De Luca, G. Celebre, M. Longeri, L. Muccioli and C. Zannoni, Order and Conformation of Biphenyl in Cyanobiphenyl Liquid Crystals: A Combined Atomistic Molecular Dynamics and ^{1}H NMR Study, *ChemPhysChem*, 2014, **15**, 1356–1367.

20 Y. Wu, H. L. Tepper and G. A. Voth, Flexible simple point-charge water model with improved liquid-state properties, *J. Chem. Phys.*, 2006, **124**, 024503.

21 L. Martínez, R. Andrade, E. G. Birgin and J. M. Martínez, PACKMOL: A package for building initial configurations for molecular dynamics simulations, *J. Comput. Chem.*, 2009, **30**, 2157–2164.

22 S. J. A. van Gisbergen, J. G. Snijders and E. J. Baerends, Calculating frequency-dependent hyperpolarizabilities using time-dependent density functional theory, *J. Chem. Phys.*, 1998, **109**, 10644–10656.

23 T. Helgaker, S. Coriani, P. Jørgensen, K. Kristensen, J. Olsen and K. Ruud, Recent Advances in Wave Function-Based Methods of Molecular-Property Calculations, *Chem. Rev.*, 2012, **112**, 543–631.

24 Y. Zhao and D. G. Truhlar, The M06 Suite of Density Functionals for Main Group Thermochemistry, Thermochemical Kinetics, Noncovalent Interactions, Excited States, and Transition Elements: two New Functionals and Systematic Testing of Four M06-Class Functionals and 12 Other Functionals, *Theor. Chem. Acc.*, 2008, **120**, 215–241.

25 L. E. Johnson, L. R. Dalton and B. H. Robinson, Optimizing Calculations of Electronic Excitations and Relative Hyperpolarizabilities of Electrooptic Chromophores, *Acc. Chem. Res.*, 2014, **47**, 3258–3265.

26 L. Lescos, S. Sitkiewicz, P. Beaujean, M. Blanchard-Desce, B. R. Champagne, E. Matito and F. Castet, Performance of DFT Functionals for Calculating the Second-Order Nonlinear Optical Properties of Dipolar Merocyanines, *Phys. Chem. Chem. Phys.*, 2020, 16579–16594.

27 B. Mennucci, R. Cammi and J. Tomasi, Medium Effects on the Properties of Chemical Systems: Electric and Magnetic Response of Donor-Acceptor Systems Within the Polarizable Continuum Model, *Int. J. Quantum Chem.*, 1999, **75**, 767–781.

28 J. Tomasi, B. Mennucci and R. Cammi, Quantum Mechanical Continuum Solvation Models, *Chem. Rev.*, 2005, **105**, 2999–3093.

29 K. Pielak, C. Tonnelé, L. Sanguinet, E. Cariati, S. Righetto, L. Muccioli, F. Castet and B. Champagne, Dynamical behavior and second harmonic generation responses in acido-triggered molecular switches, *J. Phys. Chem. C*, 2018, **122**, 26160–26168.

30 T. N. Ramos, S. Canuto and B. Champagne, Unraveling

Physical Chemistry Chemical Physics Accepted Manuscript

the Electric Field-Induced Second Harmonic Generation Responses of Stilbazolium Ion Pairs Complexes in Solution Using a Multiscale Simulation Method, *J. Chem. Inf. Model.*, 2020, **60**, 4817–4826.

31 T. N. Ramos, F. Castet and B. Champagne, Second Harmonic Generation Responses of Ion Pairs Forming Dimeric Aggregates, *J. Phys. Chem. B*, 2021, **125**, 3386–3397.

32 C. Bouquiaux, C. Tonnelé, F. Castet and B. Champagne, Second-Order Nonlinear Optical Properties of an Amphiphilic Dye Embedded in a Lipid Bilayer. A Combined Molecular Dynamics - Quantum Chemistry Study, *J. Phys. Chem. B*, 2020, **124**, 2101–2109.

33 C. Tonnelé, K. Pielak, J. Deviers, L. Muccioli, B. Champagne and F. Castet, Nonlinear optical responses of self-assembled monolayers functionalized with indolino–oxazolidine photoswitches, *Phys. Chem. Chem. Phys.*, 2018, **20**, 21590–21597.

34 C. Tonnelé, B. Champagne, L. Muccioli and F. Castet, Nonlinear Optical Contrast in Azobenzene-Based Self-Assembled Monolayers, *Chem. Mater.*, 2019, **31**, 6759–6769.

35 D. C. Ghosh and N. Islam, Semiempirical evaluation of the global hardness of the atoms of 103 elements of the periodic table using the most probable radii as their size descriptors, *Int. J. Quantum Chem.*, 2010, **110**, 1206–1213.

36 J. Seibert, B. Champagne, S. Grimme and M. de Wergifosse, Dynamic Structural Effects on the Second-Harmonic Generation of Tryptophane-Rich Peptides and Gramicidin A, *J. Phys. Chem. B*, 2020, **124**, 2568–2578.

37 R. Bersohn, Y. Pao and H. L. Frisch, Double Quantum Light Scattering by Molecules, *J. Chem. Phys.*, 1966, **45**, 3184 – 3198.

38 H. Reis, Problems in the comparison of theoretical and experimental hyperpolarizabilities revisited, *J. Chem. Phys.*, 2006, **125**, 014506.

39 J. Comer, J. C. Gumbart, J. Hénin, T. Lelièvre, A. Pohorille and C. Chipot, The Adaptive Biasing Force Method: Everything You Always Wanted To Know but Were Afraid To Ask, *J. Phys. Chem. B*, 2015, **119**, 1129–1151.

40 D. Erdemir, A. Y. Lee and A. S. Myerson, Nucleation of Crystals from Solution: Classical and Two-Step Models, *Acc. Chem. Res.*, 2009, **42**, 621–629.

41 D. Zahn, Thermodynamics and Kinetics of Prenucleation Clusters, Classical and Non-Classical Nucleation, *ChemPhysChem*, **16**, 2069–2075.

42 K. Pielak, F. Bondu, L. Sanguinet, V. Rodriguez, B. Champagne and F. Castet, Second-Order Nonlinear Optical Properties of Multiaddressable Indolinooxazolidine Derivatives: Joint Computational and Hyper-Rayleigh Scattering Investigations, *J. Phys. Chem. C*, 2017, **121**, 1851–1860.

43 J. E. Subotnik, S. Yeganeh, R. J. Cave and M. A. Ratner, Constructing diabatic states from adiabatic states: Extending generalized Mulliken–Hush to multiple charge centers with Boys localization, *J. Chem. Phys.*, 2008, **129**, 244101.

44 S. Sanyal, A. Painelli, S. K. Pati, F. Terenziani and C. Sissa, Aggregates of quadrupolar dyes for two-photon absorption: the role of intermolecular interactions, *Phys. Chem. Chem. Phys.*, 2016, **18**, 28198–28208.

45 W. Li, Q. Peng, H. Ma, J. Wen, J. Ma, L. A. Peteanu and Z. Shuai, Theoretical Investigations on the Roles of Intramolecular Structure Distortion versus Irregular Intermolecular Packing in Optical Spectra of 6T Nanoparticles, *Chem. Mater.*, 2017, **29**, 2513–2520.

46 R. Le Dantec, Y. Mugnier, G. Djanta, L. Bonacina, J. Extermann, L. Badie, C. Joulaud, M. Gerrmann, D. Rytz, J. P. Wolf and C. Galez, Ensemble and Individual Characterization of the Nonlinear Optical Properties of ZnO and BaTiO3 Nanocrystals, *J. Phys. Chem. C*, 2011, **115**, 15140–15146.

47 O. Quinet, B. Champagne and B. Kirtman, Zero-point vibrational averaging correction for second harmonic generation in para-nitroaniline, *J. Mol. Struct. (THEOCHEM)*, 2003, **633**, 199–207.

48 P. Norman, D. M. Bishop, H. J. A. Jensen and J. Oddershede, Nonlinear response theory with relaxation: The first-order hyperpolarizability, *J. Chem. Phys.*, 2005, **123**, 194103.

49 K. Kristensen, J. Kauczor, T. Kjærgaard and P. Jørgensen, Quasienergy formulation of damped response theory, *J. Chem. Phys.*, 2009, **131**, 044112.

50 J. Kauczor, P. Jørgensen and P. Norman, On the Efficiency of Algorithms for Solving Hartree–Fock and Kohn–Sham Response Equations, *J. Chem. Theory Comput.*, 2011, **7**, 1610–1630.